Electronic Supporting Information

Carboxylated MWCNT-Induced Mesoporous Fe_3O_4 Constructs Hierarchical Heterointerface Aerogels for Ultra-High-Efficiency Microwave-Terahertz Broadband Absorption

Xi Lin[a], Chenchen Wang[a], Chaoqun Zhang[a,b*], Chuanshuang Hu[a*], Yi Yang[a], Yonghui Zhou[a], Xiuyi Lin[a], Jiangtao Xu[a*]

[a] Key Laboratory of Advanced Materials for Facility Agriculture, Ministry of Agriculture, College of Materials and Energy, South China Agricultural University, Guangzhou, 510462, China

[b] College of Materials Science and Art Design, Inner Mongolia Agricultural University, Hohhot 010010, China

DFT calculations:

The computational component of this study was performed using the Density Functional Theory (DFT) software CASTEP (Cambridge Sequential Total Energy Package). For geometry optimization, the exchange-correlation functional was set to GGA-PBE (Perdew–Burke–Ernzerhof functional), and the atomic positions were relaxed using the BFGS algorithm (Limited-memory Broyden–Fletcher–Goldfarb–Shanno method). The <311> surface model was constructed with four atomic layers, in which the bottom two layers were fixed, and a vacuum layer of 15 Å was applied. For the slab, one surface layer of atoms was allowed to relax until the forces on each atom were below 10^{-4} eV·Å^{-1}. According to the measurement and calculation by Hiroki et al. [1], the work function of carbon nanotubes approaches 4.3 eV.

Electromagnetic Parameter Calculation Theories:

The Cole−Cole curve, derived from the Debye relaxation theory, enables the analysis of polarization loss. It depicts the correlation between the real and imaginary components of the permittivity, as depicted in equation S1. [2]

$$\left(\varepsilon' - \frac{\varepsilon_s + \varepsilon_\infty}{2}\right)^2 + \left(\varepsilon''\right)^2 = \left(\frac{\varepsilon_s - \varepsilon_\infty}{2}\right)^2 \#(S1)$$

Here, ε_s is the static permittivity, and ε_∞ is the relative permittivity at the limiting high frequency. Generally, each Cole−Cole semicircle corresponds to a Debye polarization process.

RL intensities can describe the EMA properties of EWAMs at different frequency points with the following equations.[3]

$$RL\ (dB) = 20\log\left|\frac{Z_{in} - 1}{Z_{in} + 1}\right| \#(S2)$$

$$Z_{in} = \sqrt{\frac{\mu_r}{\varepsilon_r}}\tan\left[j\left(\frac{2\pi}{c}\right)fd\sqrt{\mu_r\varepsilon_r}\right] \#(S3)$$

where Z_{in} represents the normalized input impedance, C is the velocity of the EMW in free space, and d is the thickness of EWAMs. The effective absorption bandwidth

(EAB) represents the frequency range where RL falls below -10 dB, indicating more than 90% attenuation of the EMWs within this range.

The α can be calculated using the following formula.

$$\alpha = \frac{\sqrt{2}\pi f}{c} \times \sqrt{\left(\mu_r''\varepsilon_r'' - \mu_r'\varepsilon_r'\right) + \sqrt{\left(\mu_r''\varepsilon_r'' - \mu_r'\varepsilon_r'\right)^2 + \left(\mu_r'\varepsilon_r'' - \mu_r''\varepsilon_r'\right)^2}} \#(S4)$$

Impedance matching can be calculated using the following formula.[4]

$$Z = \left|\frac{Z_{in}}{Z_0}\right| = \sqrt{\frac{\mu_r}{\varepsilon_r}} \tan h\left[j\left(\frac{2\pi}{c}\right) f d \sqrt{\mu_r \varepsilon_r}\right] \#(S5)$$

where d is the thickness of the absorber, and Z_0 and Z_{in} are the free space and input impedances of the absorber. When Z approaches 1 (in the range of 0.8-1.2), more EMWs are absorbed rather than reflected on the surface, which is considered a good impedance matching.

The eddy current loss coefficient (C_0) can be calculated using the following formula.[5]

$$C_0 = \mu''(\mu')^{-2} f^{-1} \#(S6)$$

Calculation process of conductive loss (ε_c'') and polarization loss (ε_P''):

According to Debye theory, the conductive loss (ε_c'') and polarization loss (ε_P'') can be precisely extracted via a nonlinear least-squares fitting method, as comprehensively demonstrated in reference. The fundamental principles of Debye theory are elucidated as follows[6]:

$$\varepsilon''(\omega) = \varepsilon_p'' + \varepsilon_c'' = (\varepsilon_s - \varepsilon_\infty)\frac{\omega\tau}{1+\omega^2\tau^2} + \frac{\sigma}{\varepsilon_0\omega} \#(S7)$$

$$\varepsilon_p'' = (\varepsilon_s - \varepsilon_\infty)\frac{\omega\tau}{1+\omega^2\tau^2} \#(S8)$$

$$\varepsilon_c'' = \frac{\sigma}{\varepsilon_0\omega} \#(S9)$$

In this context, $\omega = 2\pi f$ represents the angular frequency, with f denoting the

frequency of the electromagnetic field. τ signifies the relaxation time, which characterizes the time scale for polarization processes to reach equilibrium in response to an applied field. σ is the electrical conductivity, reflecting the material's ability to conduct electric current. ε_s stands for the static dielectric constant, indicating the material's polarization capacity under a static electric field, while ε_∞ represents the optical dielectric constant, corresponding to the material's response at very high frequencies, typically in the optical range.

The specific reference code is as follows：

```
import numpy as np
import pandas as pd
from scipy.optimize import curve_fit
import matplotlib.pyplot as plt
epsilon_0 = 8.854e-12
def calculate_conductivity(freqs_ghz, eps_imag):
    freqs_hz = np.array(freqs_ghz) * 1e9
    return 2 * np.pi * freqs_hz * epsilon_0 * np.array(eps_imag)
def conductivity_model(f_ghz, sigma_dc, A, s):
    f_hz = np.array(f_ghz) * 1e9
    return sigma_dc + A * (f_hz ** s)
def fit_sample(freqs_ghz, conductivities):
    sigma_min = np.min(conductivities)
    sigma_max = np.max(conductivities)
    bounds = ([0, 0, 0.01], [sigma_max * 1.5, sigma_max * 10, 0.99])
    p0 = [sigma_min * 0.9, (sigma_max - sigma_min) / 2, 0.7]
    try:
        popt, pcov = curve_fit(
            conductivity_model,
            freqs_ghz,
            conductivities,
```

```
            p0=p0,
            bounds=bounds,
            maxfev=5000)
        fitted_cond = conductivity_model(freqs_ghz, *popt)
        residuals = conductivities - fitted_cond
        ss_res = np.sum(residuals**2)
        ss_tot = np.sum((conductivities - np.mean(conductivities))**2)
        r_squared = 1 - (ss_res / ss_tot) if ss_tot != 0 else np.nan
        return popt, r_squared
    except Exception as e:
        print(f"Fitting failed: {str(e)}")
        return [np.nan, np.nan, np.nan], np.nan
def main(input_files):
    results = []
    for i, file in enumerate(input_files):
        df = pd.read_csv(file)
        freqs = df.iloc[:, 0].values
        eps_imag = df.iloc[:, 2].values
         cond = calculate_conductivity(freqs, eps_imag)
        popt, r2 = fit_sample(freqs, cond)
        sigma_dc, A, s = popt
        results.append({
            'sample_id': i+1,
            'sigma_dc': sigma_dc,
            'A': A,
            's': s,
            'R_squared': r2,
            'file': file})
        plt.Fig.(figsize=(10, 6))
        plt.scatter(freqs, cond, s=20)
```

```
        fit_freqs = np.linspace(min(freqs), max(freqs), 200)
        fit_cond = conductivity_model(fit_freqs, *popt)
        plt.plot(fit_freqs, fit_cond, 'r-')
        plt.title(f'Sample {i+1}')
        plt.xlabel('Frequency (GHz)')
        plt.ylabel('Conductivity (S/m)')
        plt.yscale('log')
        plt.xscale('log')
        plt.grid(True, which='both', linestyle='--')
        plt.savefig(f'sample_{i+1}_fit.png', dpi=300)
        plt.close()
    return pd.DataFrame(results)
if __name__ == "__main__":
    input_files = [f'sample_{i}.csv' for i in range(1, 8)]
    results = main(input_files)
    results.to_csv('conductivity_fitting_results.csv', index=False)
    print(results)
```

The THz shielding performance of the prepared FC600 and FCPB samples with different mixing ratios was evaluated using a terahertz time-domain spectroscopy (THz-TDS) system (CCT-1800, Huaxun Ark) in transmission and reflection modes, respectively. The effective range is 0.1-4.5 THz. Test method : Terahertz transmission method, in the nitrogen environment, the sample warehouse no-load as a reference signal (ref), terahertz transmission module test sample of terahertz spectrum, the sample to obtain two parallel data, time domain delay 54 ps, the average number of spectra : 100 ; in the terahertz reflection method, in the nitrogen environment, the planar metal aluminum plate is used as the reference signal (ref), and the terahertz spectrum of the terahertz reflection module is tested. Other test parameters are consistent with the transmission spectrum (time domain delay 54 ps, spectral average number : 100). The transmissivity (T) and reflectivity (R) were evaluated according to Equations (S10)

and (S11), respectively.[7]

$$T = \left[\frac{E_{Ts}(\omega)}{E_{Tr}(\omega)}\right]^2 = |S_{21}|^2 \#(S10)$$

$$R = \left[\frac{E_{Rs}(\omega)}{E_{Rr}(\omega)}\right]^2 = |S_{11}|^2 \#(S11)$$

where $E_{Ts}(\omega)$ and $E_{Tr}(\omega)$ refers to the electric field amplitude of sample and reference in transmission mode, respectively. And $E_{Rs}(\omega)$ and $E_{Rr}(\omega)$ refers to the amplitude of sample and reference in reflection mode, respectively.

The absorptivity (A) was obtained as follows.

$$A = 1 - T - R \#(S12)$$

The reflection loss (RL) was calculated by (S13).

$$RL = -20 \times \log_{10}\left[\frac{E_{Rs}(\omega)}{E_{Rr}(\omega)}\right] = -20\log_{10}\left(|S_{11}|\right) \#(S13)$$

Shielding effectiveness (SE) including SE_T, SE_A, and SE_R was evaluated by Equation (S14), (S15), and (S16) .[8]

$$SE_T = SE_R + SE_A = -10\log_{10} T \#(S14)$$

$$SE_R = -10\log_{10}(1 - R) \#(S15)$$

$$SE_A = -10\log_{10}(T/(1 - R)) \#(S16)$$

Where SE_T refer to the total EMI shielding effectiveness. SE_A and SE_R are the contributions of absorption and reflection.

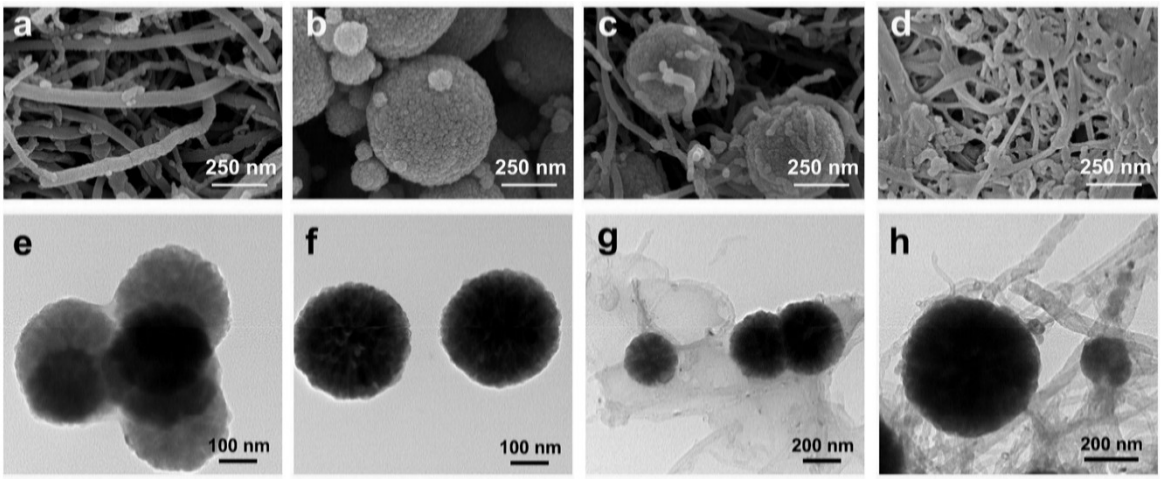

Fig. S1 SEM images of surface morphology of (a) CNT, (b) FC0, (c) FC600 and (d) PB28. TEM images of (e) FC0 (without PEG), (f) FC0, (g) FC600 (without PEG) and (h) FC600 (uncarboxylated CNTs).

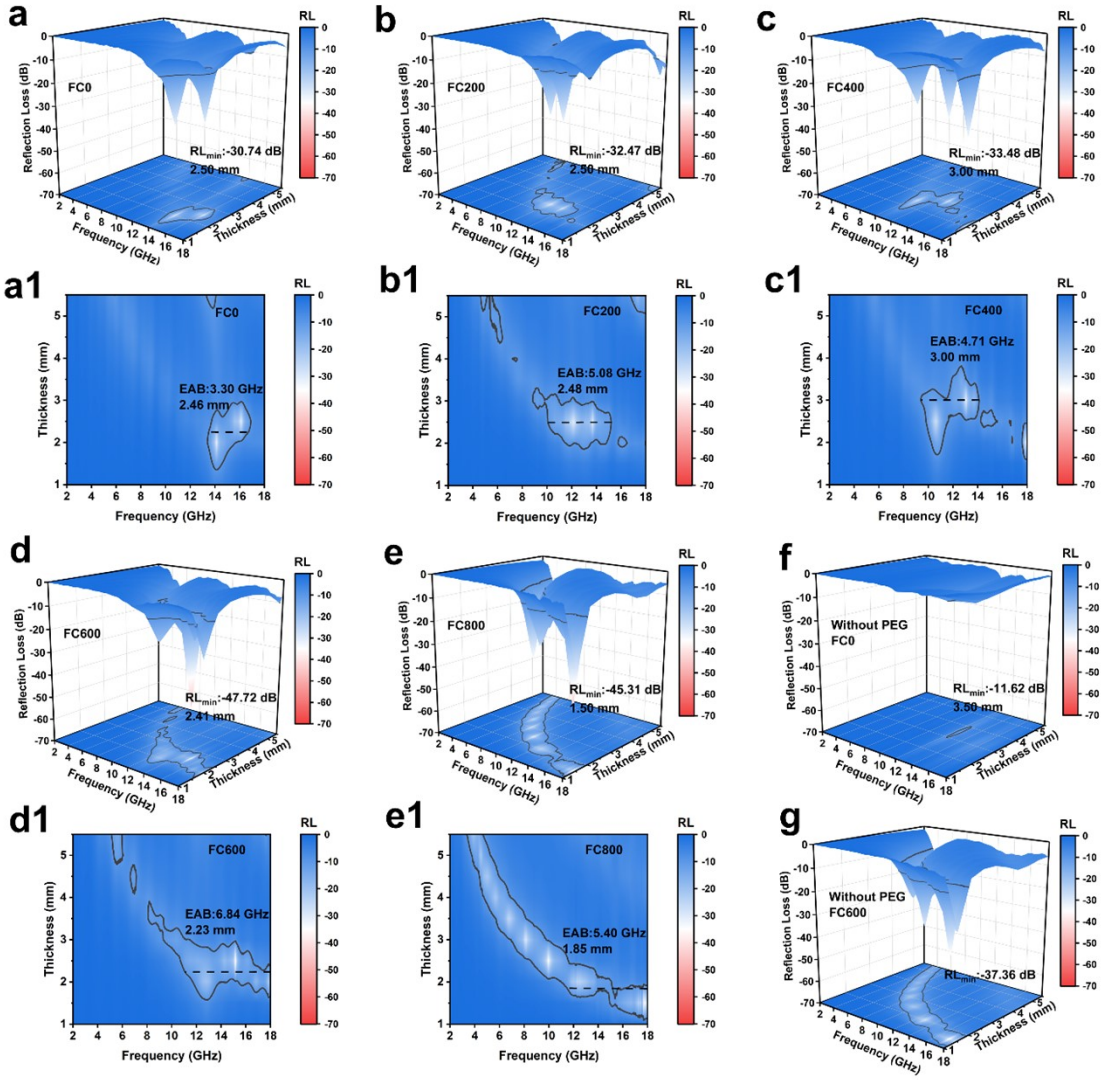

Fig. S2 3D reflection loss characterization of (a) FC0, (b) FC200, (c) FC400, (d) FC600, (e) FC800, (f) FC0 (without PEG), (g) FC600 (without PEG).

Fig. S2 demonstrates the absorptive properties of FC composites at different ratios. Compared to the unmodified FC0, PEG-modified FC0 (Fe_3O_4) exhibited an improvement in RL_{min} from -11.62 dB to -30.74 dB. This enhancement is attributed to PEG modification, which improved Fe_3O_4 dispersion and formed a protective layer on the Fe_3O_4 surface, thereby preserving its high magnetic properties. Among all samples, FC600 exhibited the most outstanding reflection loss, achieving RL_{min} of -47.72 dB at 2.41 mm and EAB of 6.84 GHz at 2.23 mm.

To thoroughly analyze the microwave absorption mechanism of FC composites, systematic investigations were conducted on the complex permittivity ($\varepsilon_r = \varepsilon' - j\varepsilon''$) and complex permeability ($\mu_r = \mu' - j\mu''$) of each FC composite. As shown in Fig. S3a, ε' generally increases with rising CNT content, attributed to the enhanced interfacial polarization effect induced by CNT's high conductivity. However, the excessively high ε' in FC800 intensifies reflection, thereby reducing RL. Fig. S3b reveals that FC600 exhibits superior relaxation loss, attributed to the mesoporous structure formed by CNT intercalated within Fe_3O_4, which enhances the interfacial polarization effect. Fig. S3c shows that all samples exhibit a significant decrease in μ' in the high-frequency region (>10 GHz), constrained by the natural resonance frequency of Fe_3O_4. The slight rebound of FC600 after its decline at 10-12 GHz suggests the presence of exchange resonance effects: the coupled interface formed between CNT and Fe_3O_4 at the nanoscale may generate exchange anisotropy, locally enhancing high-frequency magnetic response. This phenomenon was not observed in FC800, indicating that excessive CNT disrupts the effective coupling of magnetic particles. Fig. S3d shows that all samples exhibit a single-peak μ'' characteristic at high frequencies, originating from the natural resonance of Fe_3O_4. FC600 rapidly rises to its peak between 8-10 GHz, followed by a sharp decline between 10-14 GHz. This “spike” feature correlates with the superposition of multiple magnetic resonances. Overall, FC samples with varying ratios exhibit distinct electromagnetic parameters linked to the coupling effect between

CNT and Fe_3O_4. Insufficient CNT fail to regulate the dielectric-magnetic loss balance, while excessive CNT exacerbate conductive losses, thereby enhancing reflection. FC600 represents the optimized ratio for subsequent composite formation with the pure dielectric precursor PB.

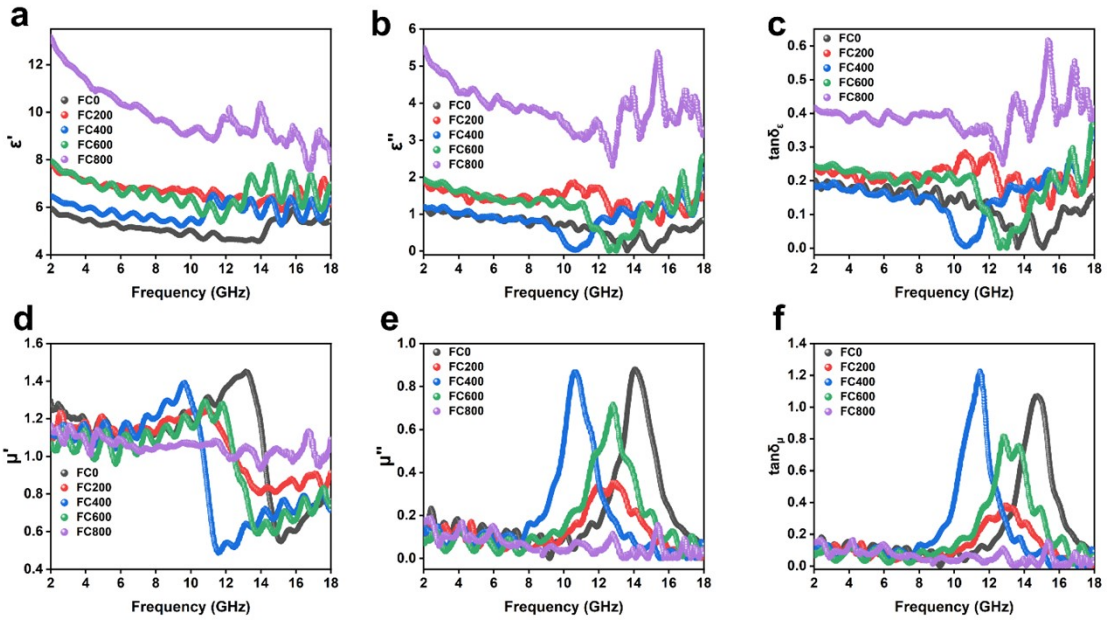

Fig. S3 The real part (a) and imaginary part (b) of permittivity, (c) Dielectric loss tangent. The real part (d) and imaginary part (e) of permeability, (f) Loss tangent of permeability.

Fig. S4 displays the absorption performance of FPB composites at different ratios. PB28 achieves an RL_{min} of -28.14 dB, whereas the best-performing FPB13 exhibits an RL_{min} of only -30.05 dB. Other FPB ratios even show a decrease in RL. The PPy@BNC surface is rich in polar groups such as hydroxyl (-OH) and pyrrole rings, while the Fe_3O_4 surface features ferric bonds (Fe-O). These surfaces interact solely via van der Waals forces, lacking the strong chemical bonding interactions. This weak interfacial bonding reduces the interface's polarization capacity during electromagnetic wave propagation, thereby diminishing the synergistic effect between dielectric and magnetic losses. To address the compatibility of interfacial bonding, carboxylated CNT were introduced during Fe_3O_4 synthesis to serve as a conductive bridging transition. These *c*-CNT form

stronger interfacial bonds with the PPy@BNC matrix through polar interactions.

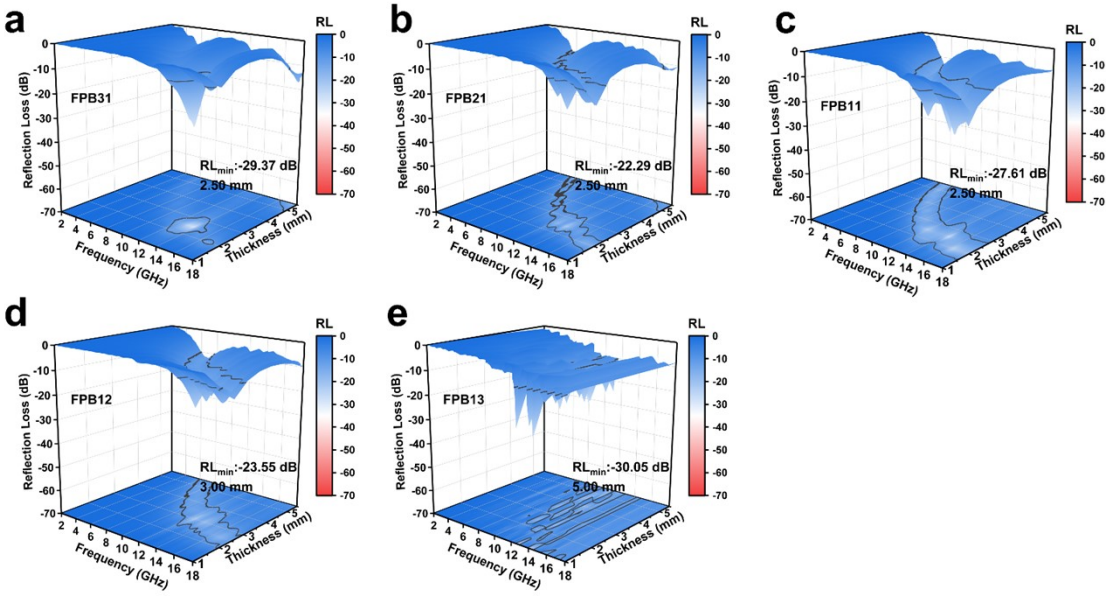

Fig. S4 3D reflection loss characterization of (a) FPB31, (b) FPB21, (c) FPB11, (d) FPB12, (e) FPB13.

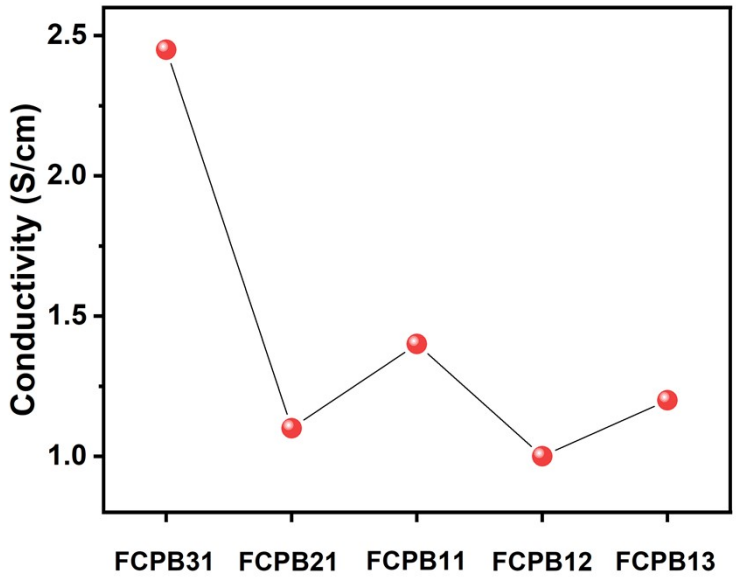

Fig. S5 Conductivity of the sample.

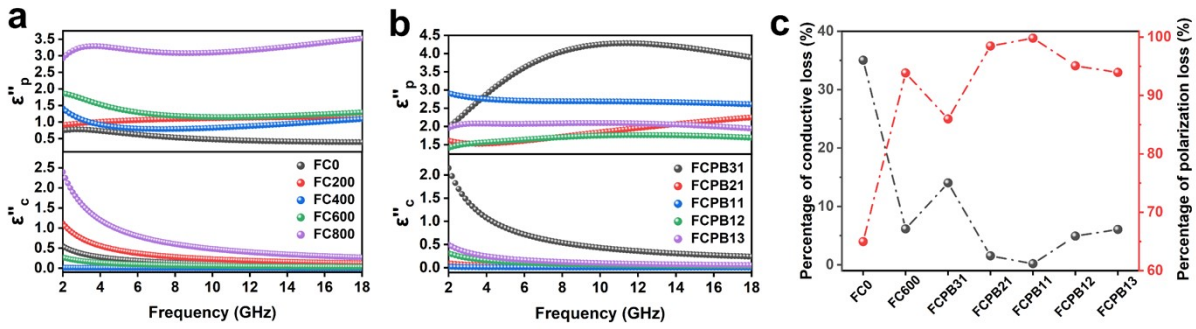

Fig. S6 (a) Polarization loss (ε''_p) and conduction loss (ε''_c) of FC. (b) Polarization loss (ε''_p) and conduction loss (ε''_p) of FCPB. (c) The proportion of conductive loss ($\varepsilon''_c/\varepsilon''$) / polarization loss $(\varepsilon''_p/\varepsilon'')$ of different samples.

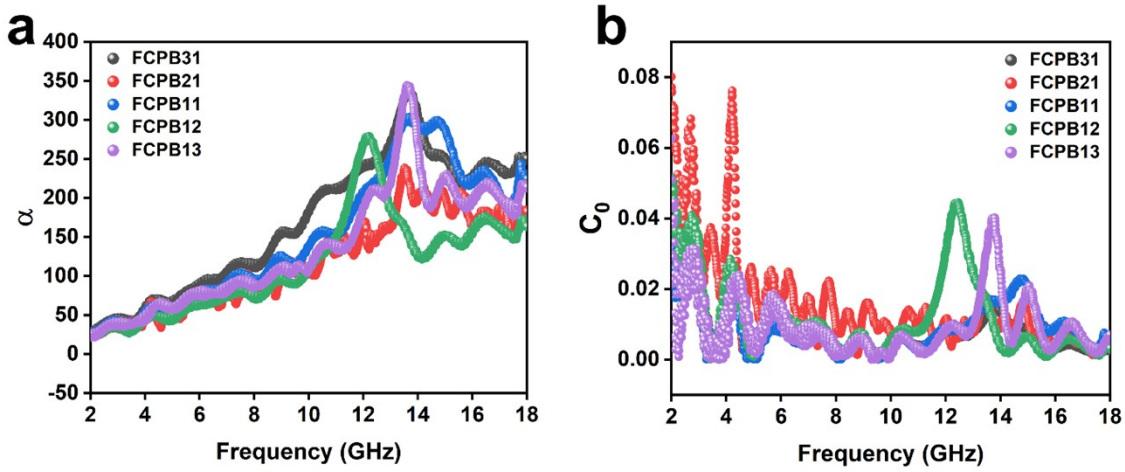

Fig. S7 (a) Attenuation constant α. (b) Eddy current loss C_0.

Fig. S8 displays the TGA curves and corresponding mass loss rate curves for FC0, FC600, and FCPB11. The mass loss of FC0 between 30-200 °C primarily stems from the volatilization of adsorbed water and residual PEG. Between 200-800 °C, the mass remains essentially stable due to the high thermal stability of Fe_3O_4 in an inert atmosphere, with no oxidation or decomposition reactions occurring. FC600 exhibits approximately 8% weight loss between 30-200 °C due to adsorbed water and PEG volatilization. From 200-600 °C, carbon nanotubes undergo gradual decomposition, with the mass loss rate increasing between 600-700 °C as the carbon skeleton of CNTs begins accelerated decomposition. The weight loss of FCPB11 at 30-150 °C stems from

water and low-boiling-point solvent volatilization. Cellulose decomposition occurs at 150-300 °C (primary weight loss phase). polypyrole decomposition occurs between 300-500 °C, and carbon nanotube oxidation decomposition takes place between 500-700 °C. Residues above 700 °C consist of Fe_3O_4 and ash.

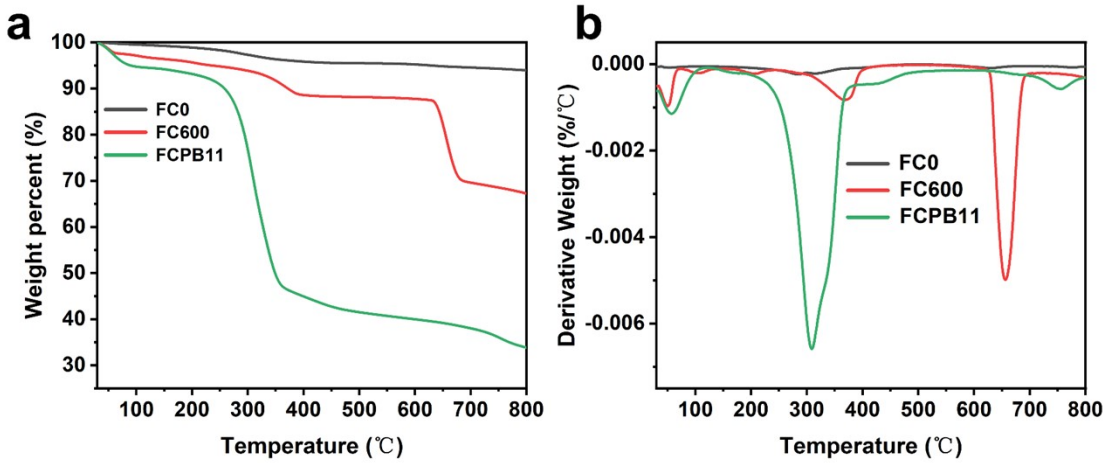

Fig. S8 (a)Thermogravimetric curve and (b)Thermogravimetric rate curve.

BET analysis shows that the composite material has a typical hierarchical porous structure with abundant micropores (concentrated in 2-4 nm) and continuous mesoporous network (mainly distributed in 4-15 nm), which provides high specific surface area (24.0540 m^2/g) and excellent mass transfer channels.

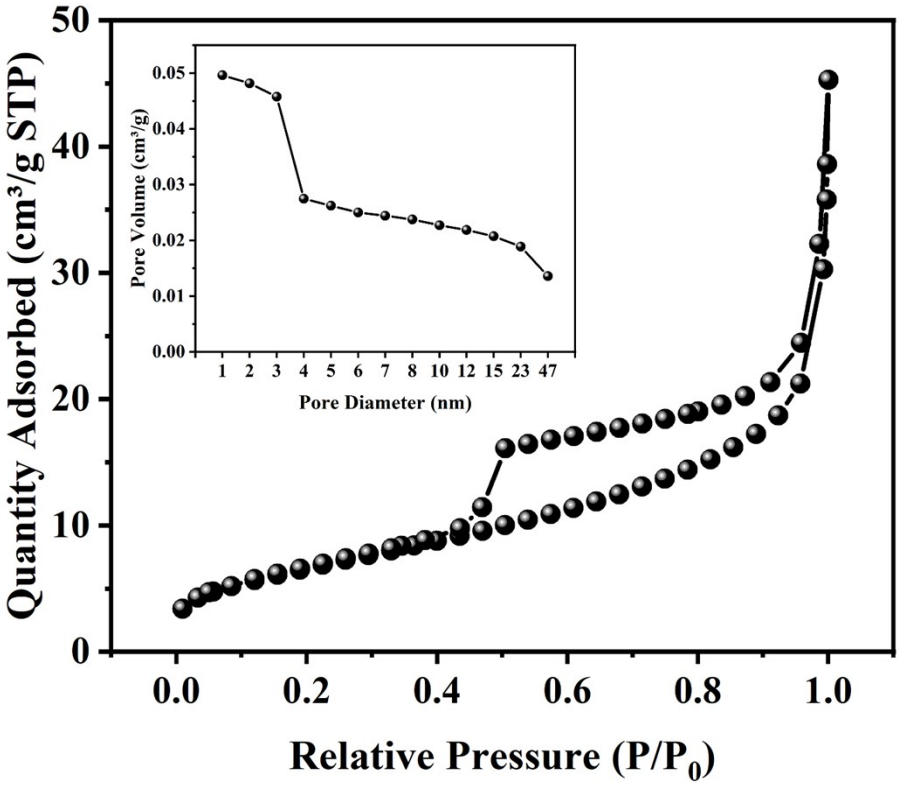

Fig. S9 BET of FCPB11.

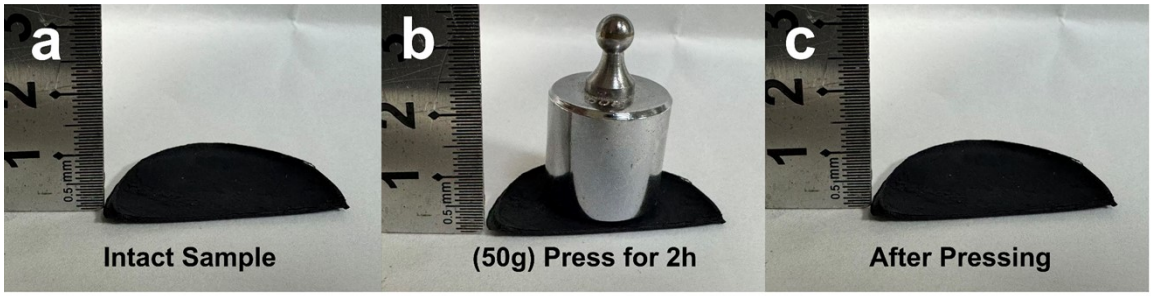

Fig. S10 Mechanical stability test of FCPB11.

Table 1

Absorbers	RL_{min}		References
	RL_{min} (dB)	Thickness (mm)	
CNFs/MXene/Fe_3O_4	-56.8 dB	2.18 mm	[9]
CF/SR	-42.2 dB	1.3 mm	[10]
Fe_3O_4/Ag	-62.3 dB	7.5 mm	[11]
Fe_3O_4/Fe/C/rGO	-65.17 dB	4.83 mm	[12]
$Fe_{16}N_2/Fe_4N$	-48.2 dB	1.3 mm	[13]
Fe/Fe_3O_4@SiO_2@Fe-2	-60.6 dB	2.2 mm	[14]
EDC@ Fe_3O_4	-54.1 dB	2.46 mm	[15]
GO/MWCNTs/Fe_3O_4	-43 dB	2.8 mm	[16]
PPy/Fe_3O_4	-45.4 dB	2.1 mm	[17]
MoS_2/PPy/rGO	-53.5 dB	2.07 mm	[18]
c-MWCNT@ Fe_3O_4-PPy@BNC	-68.51 dB	2.14 mm	This work

Table 2

Abbreviation	Full information
MWCNT	Multi-Walled Carbon Nanotube
BNC	Bacterial Nanocellulose
PPy	Polypyrrole
PB	PPy@BNC
FC	c-MWCNT@ Fe_3O_4
FPB	Fe_3O_4-PPy@ BNC
FCPB	c-MWCNT@ Fe_3O_4-PPy@BNC
Reflection loss	RL
Effective absorption bandwidth	EAB
Electromagnetic	EM
Electromagnetic wave absorber	EMWA
Microwave absorption	MA
Electromagnetic wave	EMW

References

[1] H. Ago, T. Kugler, F. Cacialli, W. R. Salaneck, M. S. P. Shaffer, A. H. Windle, R. H. Friend, *The Journal of Physical Chemistry B.* **1999**, 103, 8116.

[2] H. Dong, S. Gao, C. Yu, Z. Wang, Y. Huang, T. Zhao, Y. Li, *Composites Part B: Engineering.* **2025**, 289, 111924.

[3] X. Liu, L. Wu, J. Liu, H. Lv, P. Mou, S. Shi, L. Yu, G. Wan, G. Wang, *Carbon Energy.* **2024**, 6, e589.

[4] Y. Qian, Z. Wu, X. Lv, M. Huang, L. Rao, L. Wang, Y. Lai, J. Zhang, R. Che, *Small.* **2024**, 20, 2401878.

[5] W. Gu, S. J. H. Ong, Y. Shen, W. Guo, Y. Fang, G. Ji, Z. J. Xu, *Advanced Science.* **2022**, 9, 2204165.

[6] Z. Huang, H. Chen, Y. Huang, Z. Ge, Y. Zhou, Y. Yang, P. Xiao, J. Liang, T. Zhang, Q. Shi, G. Li, Y. Chen, *Advanced Functional Materials.* **2018**, 28, 1704363.

[7] R. Su, J. Chen, X. Zhang, W. Wang, R. He, H. Xu, Y. Li, *Chemical Engineering*

Journal. **2024**, 498, 155689.

[8] D. Yin, H. Xiu, S. Wang, Y. Pan, N. Li, R. Cheng, S. Huang, S. Fan, J. Li, *Nano Research.* **2024**, 17, 4544.

[9] X. Wang, F. Pan, L. Cai, J. Cheng, H. Jiang, Y. Yang, H. Guo, Z. Shi, Z. Xiong, A. Xie, H. Xu, W. Lu, *Chemical Engineering Journal.* **2023**, 475, 146319.

[10] Y. Liu, J. Zhou, Z. Ning, H. Huang, Z. Cheng, L. Duan, Y. Wang, X. Tao, P. Liu, Y. Ma, Z. Yao, *Advanced Functional Materials.* **2024**, 34, 2411573.

[11] X. Meng, Y. Peng, Z. Shao, X. Huang, H. Wei, Z. Wei, Q. Sun, S. Zhao, *Chemical Engineering Journal.* **2024**, 492, 152282.

[12] S. Li, Y. Sun, F. Meng, X. Jiang, H. Yu, *Chemical Engineering Journal.* **2024**, 498, 155405.

[13] J. Zheng, J. Zheng, X. Zhang, P. Yue, W. Cai, H. Chen, L. Qiao, Y. Ying, J. Yu, J. Li, W. Li, S. Che, *Advanced Functional Materials.* **2025**, 35, 2424988.

[14] C. Xu, K. Luo, Y. Du, H. Zhang, X. Lv, H. Lv, R. Zhang, C. Zhang, J. Zhang, R. Che, *Advanced Functional Materials.* **2023**, 33, 2307529.

[15] Y. Miao, M. Zhang, Q. Liu, T. Xi, Y. Liu, Y. Wang, C. Wang, A. Cui, Z. Tian, T. Wang, J. Liu, Q. Jia, D. Lan, Y. Bi, Z. Li, *Carbon.* **2025**, 235, 120076.

[16] S. Zhang, W. Li, H. Wu, J. Jiao, *Advanced Composites and Hybrid Materials.* **2023**, 6, 154.

[17] X. Yang, B. Fan, X. Tang, J. Wang, G. Tong, D. Chen, J. Guan, *Chemical Engineering Journal.* **2022**, 430, 132747.

[18] S. Liu, D. Fang, F. Xing, H. Jin, J. Li, *Chemical Engineering Journal.* **2024**, 479, 147613.